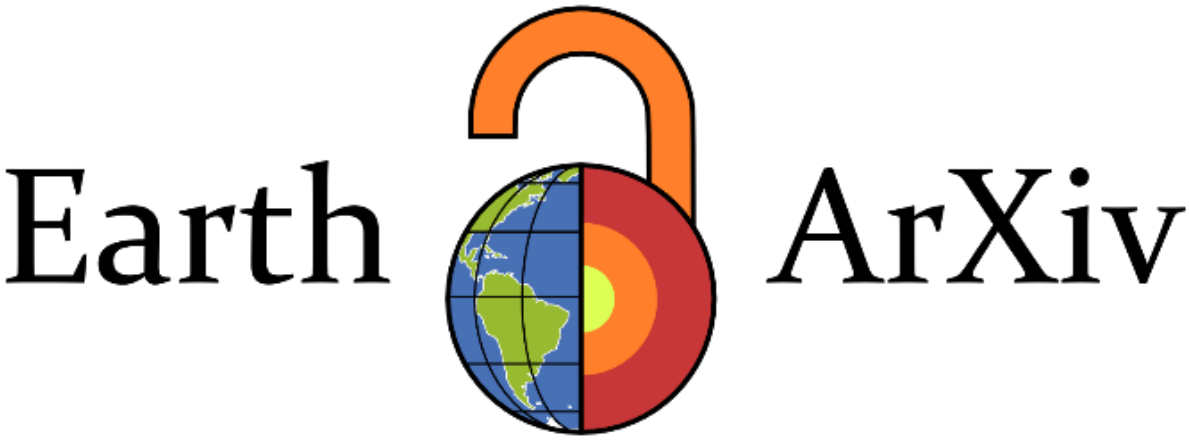

Title: Deep Neural Network-Based Inversion of Turbidites in Confined Basins

Authors: Seiya Fujishima[1], Hajime Naruse[1]

Affiliation: [1]Department of Geology and Mineralogy,
Division of Earth and Planetary Sciences, Graduate School of Science,
Kyoto University, Kyoto, Japan

Email: fujishima.seiya.z47@kyoto-u.jp

Peer review status:

This is a non-peer-reviewed preprint submitted to EarthArXiv and
has been submitted to Journal of Sedimentary Research.

Deep Neural Network-Based Inversion of Turbidites in Confined Basins

SEIYA FUJISHIMA[1] AND HAJIME NARUSE[1]

[1]Department of Geology and Mineralogy, Division of Earth and Planetary Sciences, Graduate School of Science, Kyoto University, Kyoto, Japan

Running title: DNN-BASED INVERSION OF TURBIDITES IN CONFINED BASINS

ABSTRACT

Turbidites generated by large earthquakes and other geological events are commonly preserved in small, topographically confined basins along active continental margins. Reconstructing flow conditions from these deposits is essential for assessing past hazards; however, existing inverse models have been validated only for unconfined settings, and their applicability to confined basins remains unclear. Here, we test a deep neural network (DNN)-based inverse framework using synthetic datasets generated in an idealized confined basin. Forward simulations reproduce key features of confined turbidity currents, including flow reflection and sediment ponding. Despite these complex dynamics, the trained DNN successfully reconstructs flow conditions with reasonable accuracy (SMAPE: 21.9–45.0%) using a limited number of training datasets. Notably, accurate inversion is achieved with as few as ten sampling points. These results demonstrate that inverse analysis of turbidites is feasible in confined basins even under sparse observational constraints. The proposed framework provides a practical basis for applying inverse modeling to natural deposits and offers a pathway toward linking turbidite records to the magnitude of their triggering events.

INTRODUCTION

This study proposes a novel inversion framework for reconstructing flow conditions of turbidity currents from their deposits (i.e., turbidites) in confined basins. Small scale (~10 km in diameter) submarine basins surrounded with topographic barriers are widely developed on submarine slopes in both passive and active tectonic settings, which are called confined basins or minibasin. In passive margins, salt-withdrawal minibasins along

the Gulf Coast provide well-documented examples, typically only a few tens of kilometers in diameter with subsidence rates locally exceeding 10 km/My (Winker 1996; Prather 2000; Beaubouef et al. 2003a, 2003b; Hudec et al. 2009; Prather et al. 2012). In active margins, confined basins occur in trench and forearc slope settings. For example, along the Japan Trench, subduction of the Pacific Plate has produced trench- and graben-fill basins (Strasser et al. 2023), as well as smaller basins on the forearc slope (Arai et al. 2014; Ikehara et al. 2020).

Confined basins are typically filled with turbidites and hemipelagic mudstone, and their distinctive stratigraphic patterns have attracted attention in sedimentology and petroleum geology (e.g., Felletti 2002; Khan and Imran 2008; Kane et al. 2012; Wang et al. 2017). In such settings, turbidity currents interact with surrounding topographic highs, producing distinct sedimentary architectures that differ markedly from those in unconfined systems. In unconfined basins, characteristic elements of submarine-fan models, such as leveed channels and lobes, are commonly observed (Posamentier 2003; Posamentier and Walker 2006). In contrast, minibasins such as Basin IV of the Brazos–Trinity intraslope system in the Gulf Coast lacks leveed channels and instead exhibits distributary channel complexes resembling deltaic morphology (Beaubouef et al. 2003b).

The observed differences arise from the fundamental influence of basin confinement on turbidity current dynamics. Confined basins are enclosed entirely by topographic highs that trap incoming turbidity currents, forcing interactions between inflowing currents and those reflected from downstream barriers. These interactions generate hydraulic jumps and ponding, as demonstrated by flume experiments in which a turbidity current entering a slot-like confined basin produces an upstream-migrating bore (e.g., Lamb et al. 2004; Violet et al. 2005; Toniolo et al. 2006b; Spinewine et al.

2009). These processes can be reproduced by one-dimensional layer-averaged numerical model validated against experimental data (Toniolo et al. 2006a, 2006b).

Ponding has been suggested to produce distinctive topographic features within minibasins (Violet et al. 2005; Spinewine et al. 2009). In confined basins, turbidity currents are strongly decelerated by surrounding topographic barriers, causing the flow to become ponded within the basin interior. The ponded region acts as a temporary reservoir of fine-grained suspended sediment, leading to enhanced local deposition. More recent studies have highlighted the importance of three-dimensional flow structure in ponded regions. Horizontally two-dimensional flume experiments on minibasins exhibited that the reflected flows circulate along basin margins, generating large-scale eddies (Reece et al. 2024, 2025).

These distinctive depositional process and stratigraphic architectures make confined basin deposits are important for hydrocarbon exploration and natural hazard assessment. Rapidly subsiding minibasins can trap large volumes of sandy sediment (e.g., Gulf Coast, North Sea, Precaspian Basin; Hudec and Jackson 2007). Therefore, they can trap the vast quantities of continent-derived sediment, and deposits in minibasins are expected to be high-quality reservoir rocks (Jackson et al. 2020), making them favorable sites for hydrocarbon reservoir development.

Confined basins also play key role in preserving event deposits related to geological hazards. Turbidites triggered by earthquakes, submarine landslides, and tsunamis are commonly accumulated in small, topographically confined basins along active margins (Goldfinger 2011). For example, along the Japan Trench, trench-axis basins contain turbidites correlated with major megathrust earthquakes (Ikehara et al. 2020, 2021; Strasser et al. 2023, 2024; Pizer et al. 2025), and their spatial distribution has

been used to infer past rupture extent (Strasser et al. 2024). Similar observations from the Cascadia subduction zone further indicate that isolated confined basins enable clear stratigraphic correlation of seismogenic turbidites (Goldfinger et al. 2017). These examples highlight that confined basins can preserve event deposits with high fidelity, providing valuable records of past geological hazards.

Despite their importance, the potential of confined-basin turbidites to quantitatively constrain flow conditions and triggering events remains largely unrealized. In principle, deposits accumulated within confined basins should provide valuable information on the magnitude and dynamics of turbidity currents, as well as the scale of the triggering events. Such information would be particularly useful for reconstructing flow behavior in areas where direct observations are lacking. However, no attempts have been applied to estimate quantitative flow parameters from confined basin deposits. This gap highlights a critical need for robust inversion frameworks capable of linking deposit characteristics to flow conditions in confined-basin settings.

Traditionally, the flow conditions of turbidity currents have been estimated from turbidites using deposit grain size as a proxy (e.g., Bowen et al. 1984; Komar 1985; Hiscott 1994), but mathematical optimization has led to significant advances in the inversion of turbidity currents. A one-dimensional inverse model based on a deep neural network (DNN) was proposed by Naruse and Nakao (2021) and demonstrated reasonable performance against experimental data (Cai and Naruse 2021). This DNN-based inverse model has been extended to two horizontal dimensions and successfully applied to estimate flow conditions of experimental turbidity currents at unconfined basins (Fujishima and Naruse 2026). However, this DNN-based inverse model has not yet been tested in confined basins, where turbidity currents are expected to exhibit complex flow

behaviors.

Therefore, this study aims to develop a horizontally two-dimensional DNN-based inverse model for turbidites in confined basins and to evaluate its performance. First, forward simulations were conducted to examine the sensitivity of the calculation results to the input parameters and to investigate the complex behavior of turbidity currents in confined basins. Second, inverse models were trained using various numbers of training datasets generated by the forward model. Finally, the performance of the trained inverse models was evaluated with respect to the number of training datasets, the number of sampling points, and the presence of noise in the input data.

FORWARD MODEL

Numerical model of turbidity currents

We employ a horizontally two-dimensional layer-averaged model as a forward model of turbidity currents. The forward model is based on the four-equation model proposed by Parker et al. (1986), which consists of fluid mass, fluid momentum, suspended sediment mass, and turbulent kinetic energy conservation (see Appendix for details). In this study, the original four-equation model was extended to two horizontal dimensions to represent the spreading and reflection of turbidity currents within a confined basin. To account for the settling interface of current due to particle settling, water detrainment is incorporated following Toniolo et al. (2006a).

Numerical Experiments of Ponded Turbidity Currents

Numerical simulations were conducted to investigate the dynamics of turbidity currents

and the resulting turbidite characteristics in the confined basin. The calculations were performed under the conditions of $U_0 = 2\ \mathrm{m/s}$, $C_{0,1} = C_{0,2} = 0.0025$, $h_0 = 10\mathrm{m}$ and $T_d = 432{,}000\ \mathrm{s}$, and the initial topography, the other parameters were set to the same values of calculation conditions of generation of training datasets. After the calculation, special and temporal variation of flow behavior and deposit features were observed.

Sensitivity Test

A sensitivity analysis was conducted to evaluate how the inlet parameters influence the results of forward simulations in the confined basin. Five cases were examined (Table 1): a baseline case (Case 1) and four additional cases (Cases 2–5) in each of which one of the inlet parameters ($C_{0,i}$, U_0, h_0, or T_d) was doubled relative to the baseline. Except for the modified parameter, the initial topography and all other calculation conditions were identical to those used to generate the training datasets. Differences in the resulting spatial patterns of deposit thickness were then compared among the cases.

INVERSE MODEL

Generation of Training Datasets

Numerical simulations were conducted in an idealized confined basin to generate synthetic deposits for training the inverse models (Fig. 1). The computational domain was 19 km long in the streamwise direction and 8 km in the lateral direction. The upstream slope was set to 2%, leading into a flat basin floor with a length of 12 km and a width of 4 km. On both sides of the basin floor, lateral basin slopes with a gradient of 10% and a width of 2 km were prescribed. At the downstream end, a topographic barrier was

imposed, consisting of a 10% slope with a length and width of 2 km. The inlet at the upstream boundary had a width of 1 km. The grid spacing Δx was set to 100 m in both the streamwise and lateral directions.

At the upstream boundary, the depth-averaged flow velocity, flow thickness, and suspended sediment concentration were specified as constant values during the flow duration T_d (Dirichlet boundary condition). Zero-gradient boundary conditions (Neumann boundary conditions) were applied at the downstream and lateral boundaries.

The inlet conditions were defined by the depth-averaged velocity U_0, flow thickness h_0, suspended sediment concentration for each grain-size class $C_{0,i}$, and the flow duration T_d. A continuous turbidity current was assumed such that inlet conditions were held constant over T_d. Two grain-size classes were used, with particle diameters $D_{\mathrm{s}1} = 20\ \mu\mathrm{m}$ and $D_{\mathrm{s}2} = 3\ \mu\mathrm{m}$. The values of U_0, h_0, $C_{0,i}$, and T_d were randomly sampled from uniform distributions within the ranges listed in Table 2. Each sampled parameter set was used to perform a forward simulation, and the resulting deposits were stored as elements of the training datasets.

DNN-Based Inverse Model and Training Conditions

The DNN-based inverse models were developed to estimate the input parameters of the forward model from the deposits. The model architecture was based on that used in Fujishima and Naruse (2026). The inverse models were constructed to take sediment volumes per unit area at sampling points as inputs and to infer the input parameters of the forward model (see Appendix for details). The inverse models were trained with varying numbers of training datasets, ranging from 500 to 14,500 in increments of 500, to evaluate

179 the effect of training data size on inversion performance.

180

181 ## *Evaluation of Inverse Model Performance*

182 The performance of the trained inverse models was evaluated using synthetic test datasets.
183 A total of 100 test datasets were generated independently of the training datasets, and the
184 deposit thicknesses at the same sampling points used for training were input to the inverse
185 models to estimate the model input parameters. The errors between the estimated and true
186 input parameters were then calculated using the root-mean-square error (RMSE), bias (b),
187 and symmetric mean absolute percentage error (SMAPE) as evaluation metrics. The
188 definitions of RMSE, b, SMAPE are as follows:

189 $$\mathrm{RMSE} = \sqrt{\frac{1}{N}\sum_{i}\left(y_{\mathrm{p}i} - y_i\right)^2}, \tag{21}$$

190 $$b = \frac{1}{N}\sum_{i}\left(y_{\mathrm{p}i} - y_i\right), \tag{22}$$

191 $$\mathrm{SMAPE} = \frac{100}{N}\sum_{i}\frac{2\left|y_i - y_{\mathrm{p}i}\right|}{|y_i| + \left|y_{\mathrm{p}i}\right|}, \tag{23}$$

192 where N is the number of test datasets. The variables y_i and $y_{\mathrm{p}i}$ denote the true and
193 predicted values, respectively.

194

195 ## *Effect of Sampling Point Density on Inverse Model Performance*

196 The performance of the inverse model was also evaluated as a function of sampling-point
197 density. In natural outcrops, it is often difficult to obtain laterally continuous two-
198 dimensional measurements of turbidite thickness or grain-size distributions. Therefore,
199 understanding how the inversion accuracy depends on the number of sampling locations

is essential for practical applications.

To assess this effect, the number of sampling points was varied from 10 to 50 in increments of 10, and the RMSE values for the test datasets were compared (Fig. 2). The minimum configuration of 10 points was generated by distributing the sampling locations longitudinally from upstream to downstream. Additional points were then added laterally in groups of ten to create sampling configurations of 20, 30, 40, and 50 points.

Robustness against Observation Errors

The robustness of the inverse model to observational uncertainties was also evaluated. The inversion framework in this study requires bed thickness and grain-size distributions as input; however, both measurements inevitably contain observational noise arising from coring, outcrop logging, and laboratory analyses. To assess how such uncertainties affect inversion accuracy, artificial noise was added to the test datasets, and the resulting discrepancies between the predicted and true inlet parameters were quantified.

Noise was introduced by multiplying the noise-free test data, x_{test}, by random perturbations drawn from a standard normal distribution, scaled by a noise ratio, r. Values of r ranging from 0.01 to 0.2, with increments of 0.01, were generated, corresponding to noise levels from 1% to 20% of the original data. Noisy test data, $x_{\text{test, noise}}$, were generated as:

$$x_{\text{test, noise}} = x_{\text{test}} + r\epsilon \odot x_{\text{test}}, \tag{24}$$

where the element-wise product (Hadamard product) is denoted by $\odot$, and ϵ is a vector of random values sampled from a standard normal distribution.

The inversion was performed for each r, and the SMAPE between predicted and

true input parameters of the forward model was computed. The mean SMAPE over ten independent trials was used as a measure of the robustness of the inverse model to observational noise. The mean SMAPE value was calculated as:

$$\text{Mean SMAPE} = \frac{1}{M}\sum_{m}\frac{100}{N}\sum_{n}\frac{2\left|y_{mn} - y_{\mathrm{p}mn}\right|}{\left|y_{mn}\right| + \left|y_{\mathrm{p}mn}\right|}, \tag{25}$$

where M is the number of input parameters of the forward model, y_{mn} is the true value of the nth test data set in the mth parameter, and $y_{\mathrm{p}mn}$ is the corresponding predicted value.

The inverse model for unconfined basins developed by Fujishima and Naruse (2026) was also evaluated for robustness against noisy input data, and its performance was compared with that of the present study. For this comparison, the inverse model for Run 1 of Series 1 was adopted. The inversion was performed on the test datasets from the previous study with the same range of r as described above, and the mean SMAPE was calculated. The results were then compared with those of the inverse model for a confined basin developed in this study.

RESULTS

Flow Dynamics and Depositional Patterns in Confined Basin

The example of the forward simulation exhibited that the turbidity currents in the confined basin developed complex eddies. The inflowing turbidity current reached the downstream barrier and was reflected at approximately 20,000 seconds after the start of the experiment (Fig. 3A). Following the reflection, a bore propagated upstream (Fig. 3B), and the hydraulic jump formed at the boundary between the bore and the inflowing current. The location of hydraulic jump became stabilized near the upstream slope break by

246 approximately 50,000 seconds (Fig. 3C). Eddies were generated at the location of the
247 hydraulic jump and subsequently spread throughout the basin (Fig. 3D, E, F).

248 The ponded turbidity current with large-scale eddies formed a distributary
249 channel on the basin floor. Initially, a single channel developed and migrated downstream,
250 where flow state was Froude-supercritical at around 100,000 seconds after the start of the
251 experiment (Fig. 4A, B). As the eddies developed and migrated downstream, the Froude-
252 supercritical region shifted laterally (Fig. 4C, E), resulting in the channel migration and
253 branching. The channel progressively widened, accompanied by a decrease in channel
254 depth (Fig. 4D, F).

255

256 *Sensitivity of Forward Model to Inlet Parameters*

257 Sensitivity tests of the forward model demonstrated that deposit thickness in the confined
258 basin was strongly influenced by the flow velocity at the inlet and flow duration. In the
259 baseline case (Case 1), the flow eroded the upstream slope and formed a channel-like
260 topography on the basin floor (Fig. 5A). In Case 5, where the flow duration was doubled,
261 the flow produced sinuous channel-like topography on the basin floor, reaching
262 approximately twice that in Case 1 (Fig. 5E). The calculation doubled the flow velocity
263 (Case 3) generated a channel-like topography with a wider channel than that of Case 1
264 (Fig. 5C). The suspended sediment concentration at the inlet also affected on the
265 distribution of bed thickness, but its influence was less pronounced than that of flow
266 velocity and duration. The case with doubled suspended sediment concentration (Case 2)
267 produced a channel-like topography that was similar to that of Case 1, but the bed
268 thickness was approximately doubled (Fig. 5B).

269 In contrast, flow thickness had a comparatively minor effect on the deposit

distribution. In Case 4, where h_0 was doubled, the resulting channel was slightly wider than in Case 1, but overall spatial patterns more closely resembled the Case 1 than Cases 3 or 5 (Fig. 5D).

Effect of Number of Training Datasets

The inverse model achieved satisfactory performance with a relatively small number of samples, but notable improvements were observed up to approximately 6,000 training datasets. As the number of training datasets increased, the minimum training loss decreased monotonically; however, the change was relatively small (Fig. 6). Similar to the training loss, the minimum validation loss decreased substantially as the number of training datasets increased from 500 to 6,000 and then exhibited little change beyond 6,000 datasets. These results indicate that approximately 6,000 training datasets are sufficient to achieve stable inversion performance, with little additional benefit from larger datasets. Accordingly, the inverse model used in the following analyses was trained on 6,000 datasets.

The training history for the inverse model trained with 6,000 datasets further confirmed stable convergence (Fig. 7A). The training loss rapidly decreases during the first few hundred epochs and shows little change after approximately 1,000 epochs whereas the validation loss stabilizes around 2,000 epochs. Although the validation loss was slightly higher than the training loss, the difference between them remained small, suggesting that the inverse model was sufficiently generalizable for practical use.

The trained inverse model showed good performance on the test datasets. The inlet flow velocity, U_0, and flow duration, T_d, were estimated with high accuracy, with normalized SMAPE values of 36.8% and 27.4%, respectively (Fig. 7D, F, Table 3). The

suspended sediment concentrations, $C_{0,1}$ and $C_{0,2}$, were predicted with reasonable accuracy, with SMAPE values of 32.0% and 21.9%, respectively (Fig. 7B, C, Table 3).

In contrast, the flow thickness at inlet, h_0, was slightly more difficult to estimate than the other input parameters (Fig. 7E). The parameter h_0 had a slightly higher SMAPE values than the other parameters, 45.0% (Table 3).

Influence of Sampling-Point Density and Observational Noise on the Inversion Performance

The DNN-based inverse model showed stable performance across a limited number of sampling points (Fig. 8). The minimum training loss decreased across the range of sampling points, from approximately 0.0197 to 0.0116. In contrast, the minimum validation loss showed a smaller decrease than the training loss, declining from 0.0262 to 0.0225. This small variation of validation loss suggests that the inverse model retained broadly similar predictive skill even under sparse sampling and that additional sampling points provided only limited improvement in generalization.

Moreover, the performance of the inversion does not degrade significantly for noisy input data. As the value of r increases, SMAPE shows an increasing trend: it is 32.5% at $r = 0.01$ and 41.7% at $r = 0.2$, with a difference of 9.2%. Although these values are larger than those reported by Fujishima and Naruse (2026), they exhibit a similar trend; namely, SMAPE increases monotonically as r increases. The DNN-based inverse model developed by Fujishima and Naruse (2026) shows that SMAPE increases from 27.9% to 30.1% within the range of r from 0.01 to 0.2 with a difference of 2.2% (Fig. 9). Although the inverse model in this study exhibits slightly higher SMAPE values

than that of Fujishima and Naruse (2026), it shows similar performance change over the same range of r.

DISCUSSION

Behavior of Turbidity Currents and Turbidite Features in Confined Basins

The forward model simulations in this study reproduced key dynamic characteristics of both experimental turbidity currents and field turbidites. Reece et al. (2024, 2025) conducted three-dimensional flume experiments in a topography based on salt-withdrawal minibasins on the Gulf Coast, in which they generated turbidity currents. They showed that the inflowing turbidity currents were reflected from the distal slope, generating eddies. The numerical experiments in this study also produced eddies due to reflection by the downstream barrier (Fig. 3D, E, F).

Furthermore, distributary channels have been documented in Basin IV of the Brazos–Trinity intraslope system (Beaubouef et al. 2003b; Prather et al. 2012)； similarly, our forward simulations also produced channels with unsteady pathways, resembling those formed within that minibasin (Fig. 4F).

These results imply that the forward model employed in this study successfully reproduces the actual behavior and depositional processes of turbidity currents in confined basins. Consequently, the inversion framework trained with the forward model calculation is expected to be applicable to turbidites in natural confined basins.

Performance of the Inverse Model Applied to Turbidites in Confined Basins

The most significant outcome of the inversion experiments is that the DNN-based inverse

model maintains robust predictive skill in confined basins despite limited training data, sparse sampling, and substantial observational noise. Although the forward simulations incorporate horizontally two-dimensional flow fields and complex topography, the number of training datasets required to achieve saturation in inversion accuracy is comparable to that of previous models.

Despite its higher dimensionality, the developed in this study required only a practical number of training datasets. The previous one-dimensional inverse model required more than 2,000 datasets to achieve sufficient performance (Cai and Naruse 2021; Naruse and Nakao 2021). Furthermore, the inverse model developed in this study achieved high predictive skill with a similarly practical number of training datasets. In addition, the inverse model for confined basins requires significantly fewer training datasets than the previous horizontally two-dimensional inverse model for unconfined basins, which used 10,000 training datasets (Fujishima and Naruse 2026).

Another major advantage of the proposed inversion framework is the computational efficiency of training data generation through parallel forward simulations. Because the forward simulations can be performed independently, the computational cost remains tractable, enabling the generation of sufficiently large training datasets within realistic time frames. Other inversion methods for gravity flows, such as Markov Chain Monte Carlo methods (Moretti et al. 2020; Kameda and Okamoto 2021), surrogate management methods (Lesshafft et al. 2011), genetic algorithms (Nakao et al. 2020), and interior-point line-search filter method with adjoint method (Parkinson et al. 2017), require a large number of the iterative forward simulations that cannot be easily parallelized. In contrast, the forward simulations used to generate the training datasets in the proposed framework can be fully parallelized. Therefore, our approach successfully

enables the efficient development of an inverse model of turbidites in confined basins, similar to the DNN-based inverse model for unconfined basins (Fujishima and Naruse 2026). This greatly enhances the practical applicability of the DNN-based inverse framework to natural confined basins.

One of the important outcomes of this study is the robustness of the inversion framework to observational noise. Even when random noise with a standard deviation up to 20% of the input data was introduced, the mean SMAPE did not change significantly. This tolerance indicates that the model does not depend on highly precise measurements of bed thickness but instead extracts features of spatially distributed deposits. This robustness is particularly important when applying the inverse method to confined-basin deposits in the field, because measurement errors are inevitable in measurements of bed thickness and grain-size analyses.

Differences in inversion accuracy among the reconstructed input parameters of the forward model can be interpreted in terms of the sensitivity of the forward model. Flow duration T_{d} strongly influences patterns of deposit thickness in confined basins, making it easier for the DNN to infer T_{d} from deposit features. By contrast, the flow thickness h_0 produces more subtle depositional signatures, especially on the basin plain. As a result, its reconstruction error is inherently larger. These trends are consistent with those observed in unconfined-basin inversions (Fujishima and Naruse 2026), suggesting that the DNN captures physically meaningful relationships between flow dynamics to depositional architecture.

Field Applicability and Significance of the Inversion Method Proposed in This Study

The inversion framework proposed in this study derives its predictive performance primarily from global patterns in deposit geometry rather than from fine-scale morphological details. This characteristic enables the model to remain effective even under complex and unsteady channel conditions typical of confined basins. Such complex channel morphologies are commonly observed in natural systems, for example in Basin IV of the Brazos–Trinity intraslope system (Beaubouef et al. 2003b). The ability of the inversion framework to rely on integrated depositional signals, rather than detailed channel geometry, likely explains its stable performance under these conditions.

Although natural confined basins exhibit substantial variability in geometry and formation processes, the inversion framework developed in this study can be adapted to basin-specific conditions. Basin geometry is a primary control on turbidity-current behavior, and therefore must be explicitly incorporated into inverse analysis. Natural basins display a wide range of morphologies, for example those associated with salt tectonics in the Gulf Coast, where complex minibasins and salt domes generate large variations in basin shape and depth (Kramer and Shedd 2017; Reece and Straub 2025; Reece et al. 2025). In this respect, the proposed framework is highly flexible, as it allows basin topography to be freely prescribed for individual settings.

In addition to geometry, sediment-transport pathways and source locations also vary among basins and may be poorly constrained. For example, the Hydrate Ridge west basin on the Cascadia margin lacks distinct feeder channels (Goldfinger et al. 2013). The present framework can accommodate such uncertainty because the inlet location can be treated as an output parameter, enabling inverse analysis even when sediment sources are not well defined.

The proposed inversion method is also resilient to sparse spatial sampling of

412 deposits, which is an important practical consideration for outcrop- and core-based
413 studies. In this study, as few as 30 sampling points were sufficient to perform the inversion.
414 Therefore, the inversion approach may be applicable to field-scale turbidites. For example,
415 Tokuhashi (1979) documented turbidites at 26 locations over a distance of 30 km in the
416 Kiyosumi Formation on the Boso Peninsula, Japan, and correlated them using tuffaceous
417 key beds. Such datasets satisfy the sampling requirements of the present framework,
418 suggesting that inverse analysis may be feasible for well-exposed field successions. In
419 marine core studies, the number of sampling points per basin is typically more limited.
420 However, it is possible to interpolate core data using seismic data (e.g., Kioka et al. 2019).
421 These considerations suggest that the proposed inversion framework can be realistically
422 applied to both outcrop and marine core datasets.

423 The inversion framework developed in this study provides a means to
424 quantitatively link turbidity-current dynamics to the resulting depositional architecture in
425 confined basins. Depositional features in such settings are highly variable. For example,
426 distributary channel systems are observed in minibasins in the Gulf Coast (Beaubouef et
427 al. 2003b), whereas relatively simple, laterally thinning turbidites occur in other settings
428 such as the Sorbas basin (Haughton 1994) and the Nankai Trough prism slope (Ashi et al.
429 2014). Although these differences are widely recognized, the flow conditions responsible
430 for these contrasting morphologies remain poorly constrained. By enabling the
431 reconstruction of flow parameters from deposits, the proposed inversion framework offers
432 a quantitative approach to identifying the physical controls on this depositional diversity.
433 This capability is critical because the same framework can be extended to infer the
434 magnitude of the triggering events that generate such flows.

435 Building on this capability, the inversion framework developed in this study

holds strong potential for advancing quantitative marine paleoseismology by providing constraints on the magnitude of earthquake- and tsunami-driven sediment transport processes. After the 2011 Tohoku-Oki earthquake and tsunami, turbidites were observed over a wide area of the trench slope (e.g., Arai et al. 2013; Kanamatsu et al. 2017; Ikehara et al. 2020), well as in the Japan Trench (e.g., McHugh et al. 2016; Kioka et al. 2019; Strasser et al. 2024).

Because the relationship between turbidite characteristics and earthquake magnitude is inherently indirect, a key direction for future research is therefore to integrate the present inversion framework with forward models of earthquake rupture, tsunami generation, and sediment transport. Such a coupled approach would enable reconstruction of the entire process chain, from fault slip to turbidity-current dynamics and resulting deposits. This integration would ultimately provide a pathway toward quantitative estimation of fault slip and earthquake magnitude from turbidite records, advancing the role of sedimentary archives in marine paleoseismology.

CONCLUSIONS

This study developed a horizontally two-dimensional DNN inversion framework capable of reconstructing flow conditions of turbidity currents in confined basins. Forward simulations reproduced key characteristics of confined-basin turbidity currents, including ponding and channelization.

The DNN-based inverse model demonstrated high inversion performance using a small number of training datasets. The performance of inverse model saturated at only 5,000 training datasets and successfully reconstructed the inlet conditions with reasonable accuracy. Input parameters that strongly influenced the depositional features, such as flow

velocity, suspended sediment concentration and flow duration, were estimated with high precision, whereas parameters with weaker depositional signatures, such as flow thickness, exhibited slightly larger errors.

The inversion framework exhibited notable robustness to sparse spatial sampling and observational noise, reflecting its reliance on integrated, basin-scale depositional patterns rather than fine-scale channel morphology. The inverse model required only a small number of sampling points to achieve performance saturation and showed only a 9.2% change in SMAPE under noise with a standard deviation of 0.2. This robustness suggests that the model is well-suited for applications in natural confined basins.

By enabling quantitative reconstruction of flow conditions from turbidites, the proposed framework provides a basis for linking depositional records to the processes that generate them. When integrated with models of tsunami generation, seismic shaking, and sediment transport, this approach offers a pathway toward reconstructing fault slip and earthquake magnitude from sedimentary records. Future work should focus on validating the inversion framework using experimental and natural datasets, particularly through comparison with controlled flume experiments and well-constrained field cases.

DATA AVAILABILITY STATEMENT

The training and test datasets, trained models, inversion results, and scripts to draw the figures are available on Zenodo at https://doi.org/10.5281/zenodo.19703915. The result of sensitivity test and example forward simulation were stored at https://doi.org/10.5281/zenodo.20109645. The open-source software *turb2d* (v.1.0.1) used in this study to implement the forward model is archived at https://doi.org/10.5281/zenodo.20116549 and its GitHub repository is available at

https://github.com/fujishimaseiya/turb2d. The source code for the development and verification of DNN-based inverse model for turbidity currents, *nninv1d* (v1.0.1), is archived at https://doi.org/10.5281/zenodo.20116662 and its GitHub repository is hosted at https://github.com/fujishimaseiya/nninv1d.

CONFLICTS OF INTEREST

The authors declare no conflicts of interest.

ACKNOWLEDGEMENTS

This work was supported by JST, the establishment of university fellowships towards the creation of science technology innovation (Grant Number JPMJFS2123), JST SPRING (Grant Number JPMJSP2110). Additional supports were provided by the Sediment Dynamics Research Consortium, sponsored by INPEX, JAPEX and JOGMEC.

AI STATEMENT

The authors used ChatGPT (OpenAI) and Grammarly for English language editing, including grammar correction, sentence restructuring, and improvement of readability.

REFERENCES

Arai, K., Inoue, T., Ikehara, K., and Sasaki, T., 2014, Episodic subsidence and active deformation of the forearc slope along the Japan Trench near the epicenter of the 2011 Tohoku Earthquake: Earth and Planetary Science Letters, v. 408, p. 9–15, doi:10.1016/j.epsl.2014.09.048.

507 Arai, K., Naruse, H., Miura, R., Kawamura, K., Hino, R., Ito, Y., Inazu, D.,
508 Yokokawa, M., Izumi, N., Murayama, M., and Kasaya, T., 2013, Tsunami-generated
509 turbidity current of the 2011 Tohoku-Oki earthquake: Geology, v. 41, p. 1195–1198,
510 doi:10.1130/G34777.1.
511 Ashi, J., Sawada, R., Omura, A., and Ikehara, K., 2014, Accumulation of an
512 earthquake-induced extremely turbid layer in a terminal basin of the Nankai accretionary
513 prism: Earth, Planets and Space, v. 66, p. 51, doi:10.1186/1880-5981-66-51.
514 Beaubouef, R.T., Abreu, V., and Adair, N.L., 2003a, Ultra-High Resolution 3-D
515 Characterization of Deep-Water Deposits-I: A New Approach to Understanding the
516 Stratigraphic Evolution of Intra-Slope Depositional Systems: AAPG Annual Meeting,
517 Search and Discovery Article, p. 40084.
518 Beaubouef, R.T., Wagoner, J.C.V., and Adair, N.L., 2003b, Ultra-High
519 Resolution 3-D Characterization of Deep-Water Deposits-II: Insights into the Evolution
520 of a Submarine Fan and Comparisons with River Deltas: AAPG Annual Meeting, Search
521 and Discovery Article, p. 40085.
522 Bowen, A.J., Normark, W.R., and Piper, D.J.W., 1984, Modelling of turbidity
523 currents on Navy Submarine Fan, California Continental Borderland: Sedimentology, v.
524 31, p. 169–185, doi:10.1111/j.1365-3091.1984.tb01957.x.
525 Cai, Z., and Naruse, H., 2021, Inverse Analysis of Experimental Scale Turbidity
526 Currents Using Deep Learning Neural Networks: Journal of Geophysical Research: Earth
527 Surface, v. 126, p. e2021JF006276, doi:10.1029/2021JF006276.
528 Felletti, F., 2002, Complex bedding geometries and facies associations of the
529 turbiditic fill of a confined basin in a transpressive setting (Castagnola Fm., Tertiary
530 Piedmont Basin, NW Italy): Sedimentology, v. 49, p. 645–667, doi:10.1046/j.1365-

3091.2002.00467.x.

Fujishima, S., and Naruse, H., 2026, Experimental Verification of a Two-Dimensional Inverse Method for Turbidity Currents Using a Deep Neural Network: Journal of Geophysical Research: Machine Learning and Computation, v. 3, p. e2025JH000952, doi:10.1029/2025JH000952.

Goldfinger, C., 2011, Submarine Paleoseismology Based on Turbidite Records: Annual Review of Marine Science, v. 3, p. 35–66, doi:10.1146/annurev-marine-120709-142852.

Goldfinger, C., Galer, S., Beeson, J., Hamilton, T., Black, B., Romsos, C., Patton, J., Nelson, C.H., Hausmann, R., and Morey, A., 2017, The importance of site selection, sediment supply, and hydrodynamics: A case study of submarine paleoseismology on the northern Cascadia margin, Washington USA: Marine Geology, v. 384, p. 4–46, doi:10.1016/j.margeo.2016.06.008.

Goldfinger, C., Morey, A.E., Black, B., Beeson, J., Nelson, C.H., and Patton, J., 2013, Spatially limited mud turbidites on the Cascadia margin: segmented earthquake ruptures? Natural Hazards and Earth System Sciences, v. 13, p. 2109–2146, doi:10.5194/nhess-13-2109-2013.

Haughton, P.D.W., 1994, Deposits of Deflected and Ponded Turbidity Currents, Sorbas Basin, Southeast Spain: Journal of Sedimentary Research, v. A64, p. 233–246, doi:10.1306/D4267D6B-2B26-11D7-8648000102C1865D.

Hiscott, R.N., 1994, Loss of capacity, not competence, as the fundamental process governing deposition from turbidity currents: Journal of Sedimentary Research, v. A64, p. 209–214, doi:10.2110/jsr.64.209.

Hudec, M.R., and Jackson, M.P.A., 2007, Terra infirma: Understanding salt

555 tectonics: Earth-Science Reviews, v. 82, p. 1–28, doi:10.1016/j.earscirev.2007.01.001.
556 Hudec, M.R., Jackson, M.P.A., and Schultz-Ela, D.D., 2009, The paradox of minibasin
557 subsidence into salt: Clues to the evolution of crustal basins: GSA Bulletin, v. 121, p.
558 201–221, doi:10.1130/B26275.1.
559 Ikehara, K., Usami, K., Irino, T., Omura, A., Jenkins, R.G., and Ashi, J., 2021,
560 Characteristics and distribution of the event deposits induced by the 2011 Tohoku-oki
561 earthquake and tsunami offshore of Sanriku and Sendai, Japan: Sedimentary Geology, v.
562 411, p. 105791, doi:10.1016/j.sedgeo.2020.105791.
563 Ikehara, K., Usami, K., and Kanamatsu, T., 2020, Repeated occurrence of
564 surface-sediment remobilization along the landward slope of the Japan Trench by great
565 earthquakes: Earth, Planets and Space, v. 72, p. 114, doi:10.1186/s40623-020-01241-y.
566 Jackson, C.A.-L., Duffy, O.B., Fernandez, N., Dooley, T.P., Hudec, M.R.,
567 Jackson, M.P.A., and Burg, G., 2020, The stratigraphic record of minibasin subsidence,
568 Precaspian Basin, Kazakhstan: Basin Research, v. 32, p. 739–763, doi:10.1111/bre.12393.
569 Kameda, J., and Okamoto, A., 2021, 1-D inversion analysis of a shallow
570 landslide triggered by the 2018 Eastern Iburi earthquake in Hokkaido, Japan: Earth,
571 Planets and Space, v. 73, p. 116, doi:10.1186/s40623-021-01443-y.
572 Kanamatsu, T., Usami, K., McHugh, C.M.G., and Ikehara, K., 2017, High-
573 resolution chronology of sediment below CCD based on Holocene paleomagnetic secular
574 variations in the Tohoku-oki earthquake rupture zone: Geochemistry, Geophysics,
575 Geosystems, v. 18, p. 2990–3002, doi:10.1002/2017GC006878.
576 Kane, I.A., McGee, D.T., and Jobe, Z.R., 2012, Halokinetic effects on submarine
577 channel equilibrium profiles and implications for facies architecture: conceptual model
578 illustrated with a case study from Magnolia Field, Gulf of Mexico: Geological Society,

579 London, Special Publications, v. 363, p. 289–302, doi:10.1144/SP363.13.

580 Khan, S.M., and Imran, J., 2008, Numerical Investigation of Turbidity Currents
581 Flowing Through Minibasins on the Continental Slope: Journal of Sedimentary Research,
582 v. 78, p. 245–257, doi:10.2110/jsr.2008.031.

583 Kioka, A., Schwestermann, T., Moernaut, J., Ikehara, K., Kanamatsu, T.,
584 Eglinton, T.I., and Strasser, M., 2019, Event Stratigraphy in a Hadal Oceanic Trench: The
585 Japan Trench as Sedimentary Archive Recording Recurrent Giant Subduction Zone
586 Earthquakes and Their Role in Organic Carbon Export to the Deep Sea: Frontiers in Earth
587 Science, v. 7, p. 319, doi:10.3389/feart.2019.00319.

588 Komar, P.D., 1985, The hydraulic interpretation of turbidites from their grain
589 sizes and sedimentary structures: Sedimentology, v. 32, p. 395–407, doi:10.1111/j.1365-
590 3091.1985.tb00519.x.

591 Kramer, K.V., and Shedd, W.W., 2017, A 1.4-Billion-Pixel Map of the Gulf of
592 Mexico Seafloor: Eos, v. 98, doi:10.1029/2017EO073557.

593 Lamb, M.P., Hickson, T., Marr, J.G., Sheets, B., Paola, C., and Parker, G., 2004,
594 Surging Versus Continuous Turbidity Currents: Flow Dynamics and Deposits in an
595 Experimental Intraslope Minibasin: Journal of Sedimentary Research, v. 74, p. 148–155,
596 doi:10.1306/062103740148.

597 Lesshafft, L., Meiburg, E., Kneller, B., and Marsden, A., 2011, Towards inverse
598 modeling of turbidity currents: The inverse lock-exchange problem: Computers &
599 Geosciences, v. 37, p. 521–529, doi:10.1016/j.cageo.2010.09.015.

600 McHugh, C.M., Kanamatsu, T., Seeber, L., Bopp, R., Cormier, M.-H., and Usami,
601 K., 2016, Remobilization of surficial slope sediment triggered by the A.D. 2011 Mw 9
602 Tohoku-Oki earthquake and tsunami along the Japan Trench: Geology, v. 44, p. 391–394,

603 doi:10.1130/G37650.1.

604 Moretti, L., Mangeney, A., Walter, F., Capdeville, Y., Bodin, T., Stutzmann, E.,
605 and Le Friant, A., 2020, Constraining landslide characteristics with Bayesian inversion of
606 field and seismic data: Geophysical Journal International, v. 221, p. 1341–1348,
607 doi:10.1093/gji/ggaa056.

608 Nakao, K., Naruse, H., and Tokuhashi, S., 2020, Inverse analysis to reconstruct
609 hydraulic conditions of non-steady turbidity currents: Application to an ancient turbidite
610 of the Kiyosumi Formation of the Awa Group, Boso Peninsula, central Japan: EarthArXiv,
611 doi:10.31223/X51S3S.

612 Naruse, H., and Nakao, K., 2021, Inverse modeling of turbidity currents using
613 an artificial neural network approach: verification for field application: Earth Surface
614 Dynamics, v. 9, p. 1091–1109, doi:10.5194/esurf-9-1091-2021.

615 Parker, G., Fukushima, Y., and Pantin, H.M., 1986, Self-accelerating turbidity
616 currents: Journal of Fluid Mechanics, v. 171, p. 145, doi:10.1017/S0022112086001404.

617 Parkinson, S.D., Funke, S.W., Hill, J., Piggott, M.D., and Allison, P.A., 2017,
618 Application of the adjoint approach to optimise the initial conditions of a turbidity current
619 with the AdjointTurbidity 1.0 model: Geoscientific Model Development, v. 10, p. 1051–
620 1068, doi:10.5194/gmd-10-1051-2017.

621 Pizer, C., Ikehara, K., Keep, M., Kioka, A., Kodaira, S., Miura, R., Moernaut, J.,
622 Nakamura, Y., and Strasser, M., 2025, Geological evidence for repeated slip-to-the-trench
623 style megathrust earthquakes at the Japan Trench: Geology, v. 53, p. 370–374,
624 doi:10.1130/G52797.1.

625 Posamentier, H.W., 2003, Depositional elements associated with a basin floor
626 channel-levee system: case study from the Gulf of Mexico: Marine and Petroleum

627 Geology, v. 20, p. 677–690, doi:10.1016/j.marpetgeo.2003.01.002.
628 Posamentier, H.W., and Walker, R.G., 2006, Deep-Water Turbidites and
629 Submarine Fans, *in* Posamentier, H.W. and Walker, R.G. eds., Facies Models Revisited:
630 SEPM, SEPM Special Publication 84, p. 397–520, doi:10.2110/pec.06.84.0399.
631 Prather, B.E., 2000, Calibration and visualization of depositional process models
632 for above-grade slopes: a case study from the Gulf of Mexico: Marine and Petroleum
633 Geology, v. 17, p. 619–638, doi:10.1016/S0264-8172(00)00015-5.
634 Prather, B.E., Pirmez, C., and Winker, C.D., 2012, Stratigraphy of Linked
635 Intraslope Basins: Brazos–Trinity System Western Gulf of Mexico, *in* Prather, B.E.,
636 Deptuck, M.E., Mohrig, D., Hoorn, B.V., and Wynn, R.B. eds., Application of the
637 Principles of Seismic Geomorphology to Continental Slope and Base-of-Slope Systems:
638 Case Studies from SeaFloor and Near-Sea Floor Analogues: SEPM, SEPM Special
639 Publication 99, p. 83–109, doi:10.2110/pec.12.99.0083.
640 Reece, J.K., Dorrell, R.M., and Straub, K.M., 2024, Circulation of hydraulically
641 ponded turbidity currents and the filling of continental slope minibasins: Nature
642 Communications, v. 15, p. 2075, doi:10.1038/s41467-024-46120-2.
643 Reece, J.K., Dorrell, R.M., and Straub, K.M., 2025, Influence of flow discharge
644 and minibasin shape on the flow behavior and depositional mechanics of ponded turbidity
645 currents: Geological Society of America Bulletin, v. 137, p. 1797–1814,
646 doi:10.1130/B37517.1.
647 Reece, J.K., and Straub, K.M., 2025, Statistics of Depressions Covering the
648 Northern Gulf of Mexico Salt-Minibasin Province: Drivers and Strength of Bathymetric
649 Self-Organization: Journal of Geophysical Research: Oceans, v. 130, p. e2024JC021726,
650 doi:10.1029/2024JC021726.

651 Spinewine, B., Sequeiros, O.E., Garcia, M.H., Beaubouef, R.T., Sun, T., Savoye,
652 B., and Parker, G., 2009, Experiments on Wedge-Shaped Deep Sea Sedimentary Deposits
653 in Minibasins and/or on Channel Levees Emplaced by Turbidity Currents. Part II.
654 Morphodynamic Evolution of the Wedge and of the Associated Bedforms: Journal of
655 Sedimentary Research, v. 79, p. 608–628, doi:10.2110/jsr.2009.065.
656 Strasser, M., Ikehara, K., Everest, J., Maeda, L., Hochmuth, K., Grant, H.,
657 Stewart, M., Okutsu, N., Sakurai, N., Yokoyama, T., Bao, R., Bellanova, P., Brunet, M.,
658 Cai, Z., Cattaneo, A., Hsiung, K.-H., Huang, J.-J., Ishizawa, T., Itaki, T., Jitsuno, K.,
659 Johnson, J.E., Kanamatsu, T., Keep, M., Kioka, A., Kölling, M., Luo, M., März, C.,
660 McHugh, C., Micallef, A., Nagahashi, Y., Pandey, D.K., Proust, J.-N., Rasbury, E.T.,
661 Riedinger, N., Satoguchi, Y., Sawyer, D.E., Seibert, C., Silver, M., Straub, S.M., Virtasalo,
662 J., Wang, Y., Wu, T.-W., and Zellers, S.D., 2023, Expedition 386 summary, *in* Strasser,
663 M., Ikehara, K., Everest, J., and Expedition 386 Scientists eds., Japan Trench
664 Paleoseismology: International Ocean Discovery Program, Proceedings of the
665 International Ocean Discovery Program 386, doi:10.14379/iodp.proc.386.2023.
666 Strasser, M., Ikehara, K., Pizer, C., Itaki, T., Satoguchi, Y., Kioka, A., McHugh,
667 C., Proust, J.-N., Sawyer, D., IODP Expedition Management Team, and IODP Expedition
668 386 Expedition Science Party, 2024, Japan Trench event stratigraphy: First results from
669 IODP giant piston coring in a deep-sea trench to advance subduction zone
670 paleoseismology: Marine Geology, v. 477, p. 107387, doi:10.1016/j.margeo.2024.107387.
671 Tokuhashi, S., 1979, Three Dimensional Analysis of a Large Sandy-Flysch Body,
672 Mio-Pliocene Kiyosumi Formation, Boso Peninsula, Japan: Memoirs of the Faculty of
673 Science, Kyoto University. Series of geology and mineralogy, v. 46, p. 1–60.
674 Toniolo, H., Lamb, M., and Parker, G., 2006a, Depositional Turbidity Currents

675 in Diapiric Minibasins on the Continental Slope: Formulation and Theory: Journal of
676 Sedimentary Research, v. 76, p. 783–797, doi:10.2110/jsr.2006.071.
677 Toniolo, H., Parker, G., Voller, V., and Beaubouef, R.T., 2006b, Depositional
678 Turbidity Currents in Diapiric Minibasins on the Continental Slope: Experiments—
679 Numerical Simulation and Upscaling: Journal of Sedimentary Research, v. 76, p. 798–
680 818, doi:10.2110/jsr.2006.072.
681 Violet, J., Sheets, B., Pratson, L., Paola, C., Beaubouef, R., and Parker, G., 2005,
682 Experiment on Turbidity Currents and Their Deposits in a Model 3D Subsiding
683 Minibasin: Journal of Sedimentary Research, v. 75, p. 820–843, doi:10.2110/jsr.2005.065.
684 Wang, X., Luthi, S.M., Hodgson, D.M., Sokoutis, D., Willingshofer, E., and
685 Groenenberg, R.M., 2017, Turbidite stacking patterns in salt-controlled minibasins:
686 Insights from integrated analogue models and numerical fluid flow simulations:
687 Sedimentology, v. 64, p. 530–552, doi:10.1111/sed.12313.
688 Winker, C.D., 1996, High-Resolution Seismic Stratigraphy of a Late Pleistocene
689 Submarine Fan Ponded by Salt-Withdrawal Mini-Basins on the Gulf of Mexico
690 Continental Slope: Offshore Technology Conference, Proceedings Papers, p. OTC-8024-
691 MS, doi:10.4043/8024-MS.
692
693 FIG. 1.--- Initial topography for forward simulations of turbidity currents.
694 FIG. 2.--- Sampling points used for validation of the inverse model under different
695 sampling point densities. A) 10 points. B) 20 points. C) 30 points. D) 40 points. E) 50
696 points.
697 FIG. 3.--- Spatial and temporal variations in flow thickness in the example
698 calculation at A) 20,000 seconds, B) 25,000 seconds, C) 50,000 seconds, D) 100,000

699 seconds, E) 200,000 seconds, and F) 300,000 seconds after the start of the calculation.

700 FIG. 4.--- Spatial and temporal variations in densimetric Froude number and bed
701 thickness in the example calculation. A) Densimetric Froude number and B) Bed
702 thickness at 100,000 seconds. C) Densimetric Froude number and D) bed thickness at
703 200,000 seconds. E) Densimetric Froude number and F) bed thickness at 300,000 seconds.

704 FIG. 5.--- Effect of forward model input parameters on simulated bed thickness.
705 Each panel shows the distribution of bed thickness at the end of the simulation. A) Case
706 1 (base case). B) Case 2 (double suspended-sediment concentration). C) Case 3 (double
707 flow velocity). D) Case 4 (double flow thickness). E) Case 5 (double flow duration).

708 FIG. 6--- Variation in inverse model performance with the number of training
709 data.

710 FIG. 7--- Training and test results of the inverse model trained on 6,000 datasets.
711 A) Training history on 6,000 training datasets. B–F) show the estimation accuracy of the
712 input parameters for the test datasets: B) Suspended sediment concentration (20 μm) at
713 the inlet; C) Suspended sediment concentration (3 μm) at the inlet; D) Flow velocity at
714 the inlet; E) Flow thickness at the inlet; F) Flow duration. The diagonal orange lines in
715 B–F) indicate where the original values equal the reconstructed values. Points lying on
716 these lines represent estimates with zero error.

717 FIG. 8--- Effect of the number of sampling points on inverse model performance.

718 FIG. 9--- Performance of the inverse model for noisy input data. For each value
719 of r, 10 sets of noisy data were generated to estimate the input parameters, and the
720 average SMAPE was calculated.

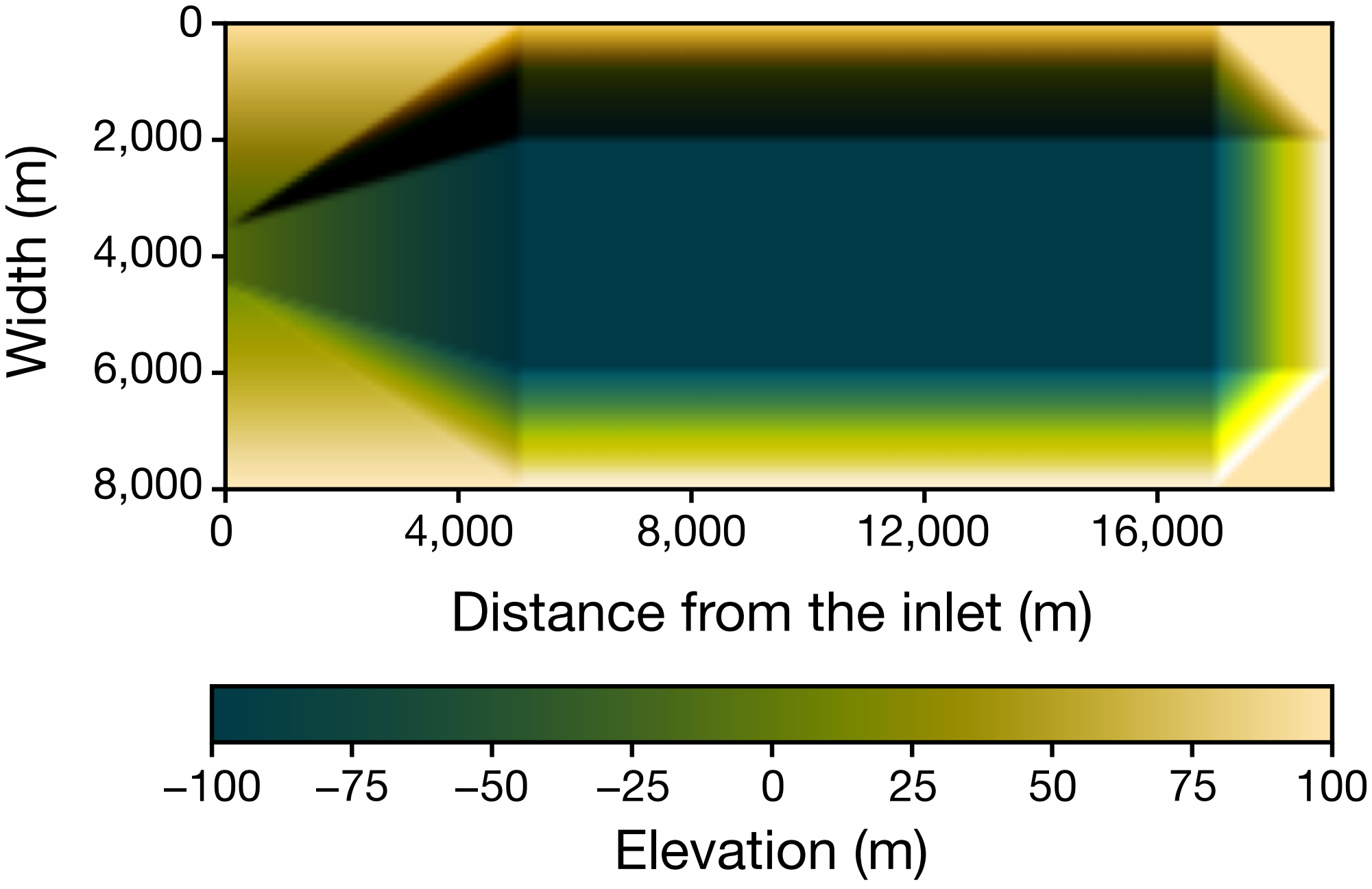
0
2,000
4,000
6,000
8,000
Width (m)
0
4,000
8,000
12,000
16,000
Distance from the inlet (m)
–100
–75
–50
–25
0
25
50
75
100
Elevation (m)

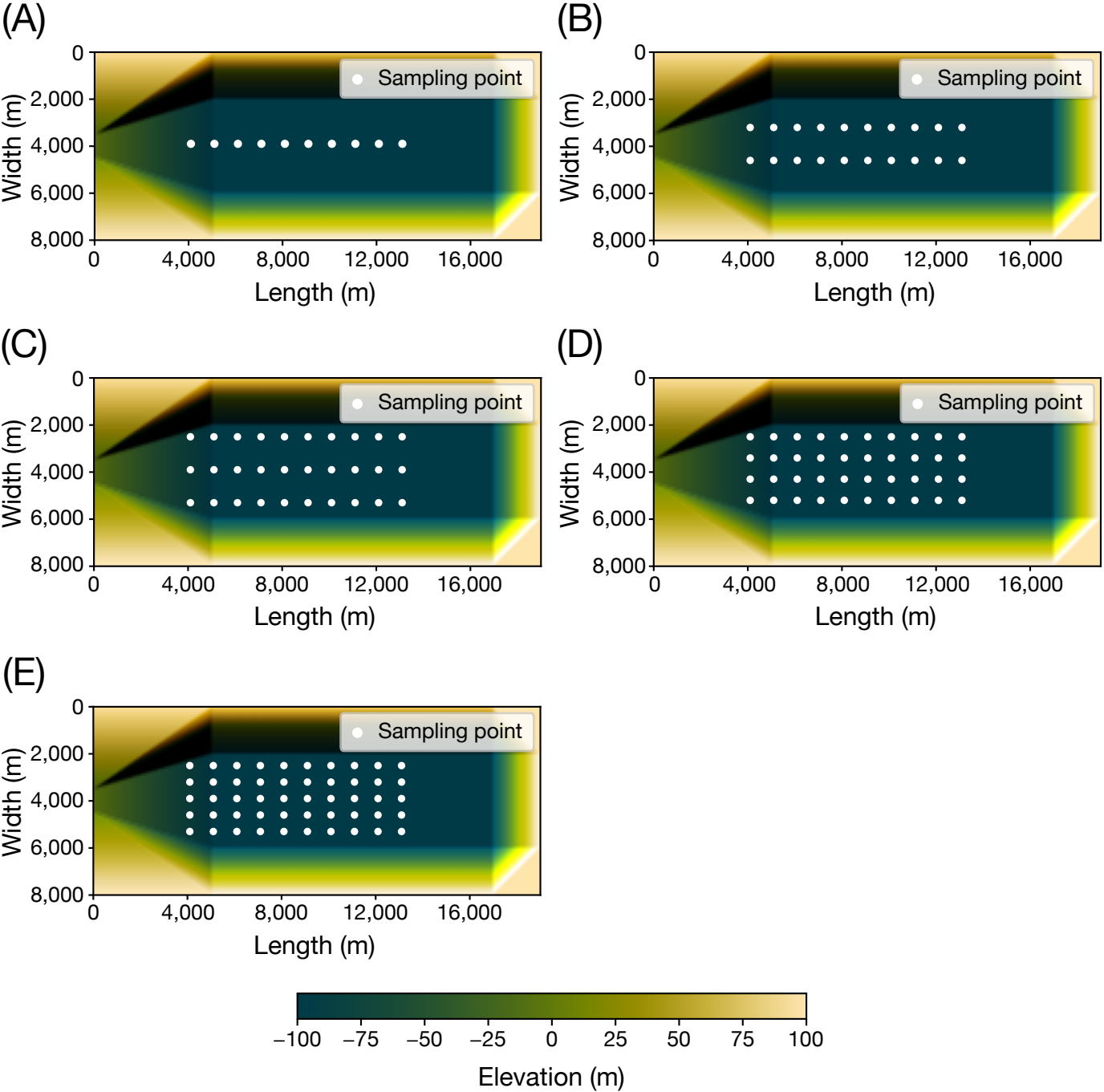
(A)
(B)
(C)
(D)
(E)
Sampling point
Width (m)
0
2,000
4,000
6,000
8,000
Length (m)
0
4,000
8,000
12,000
16,000
−100
−75
−50
−25
0
25
50
75
100
Elevation (m)

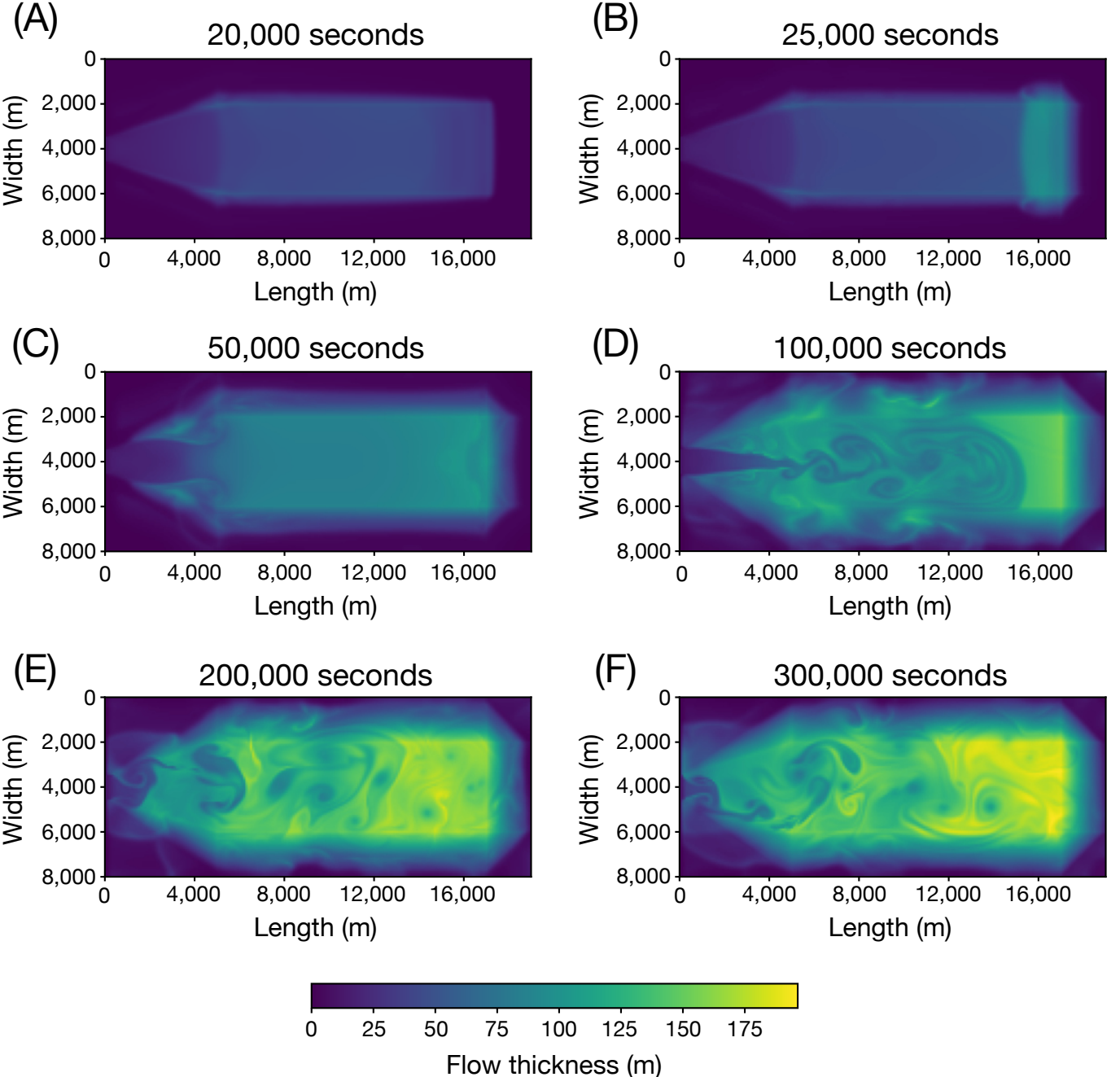
(A)
20,000 seconds
(B)
25,000 seconds
(C)
50,000 seconds
(D)
100,000 seconds
(E)
200,000 seconds
(F)
300,000 seconds
Width (m)
0
2,000
4,000
6,000
8,000
Length (m)
0
4,000
8,000
12,000
16,000
Flow thickness (m)
0
25
50
75
100
125
150
175

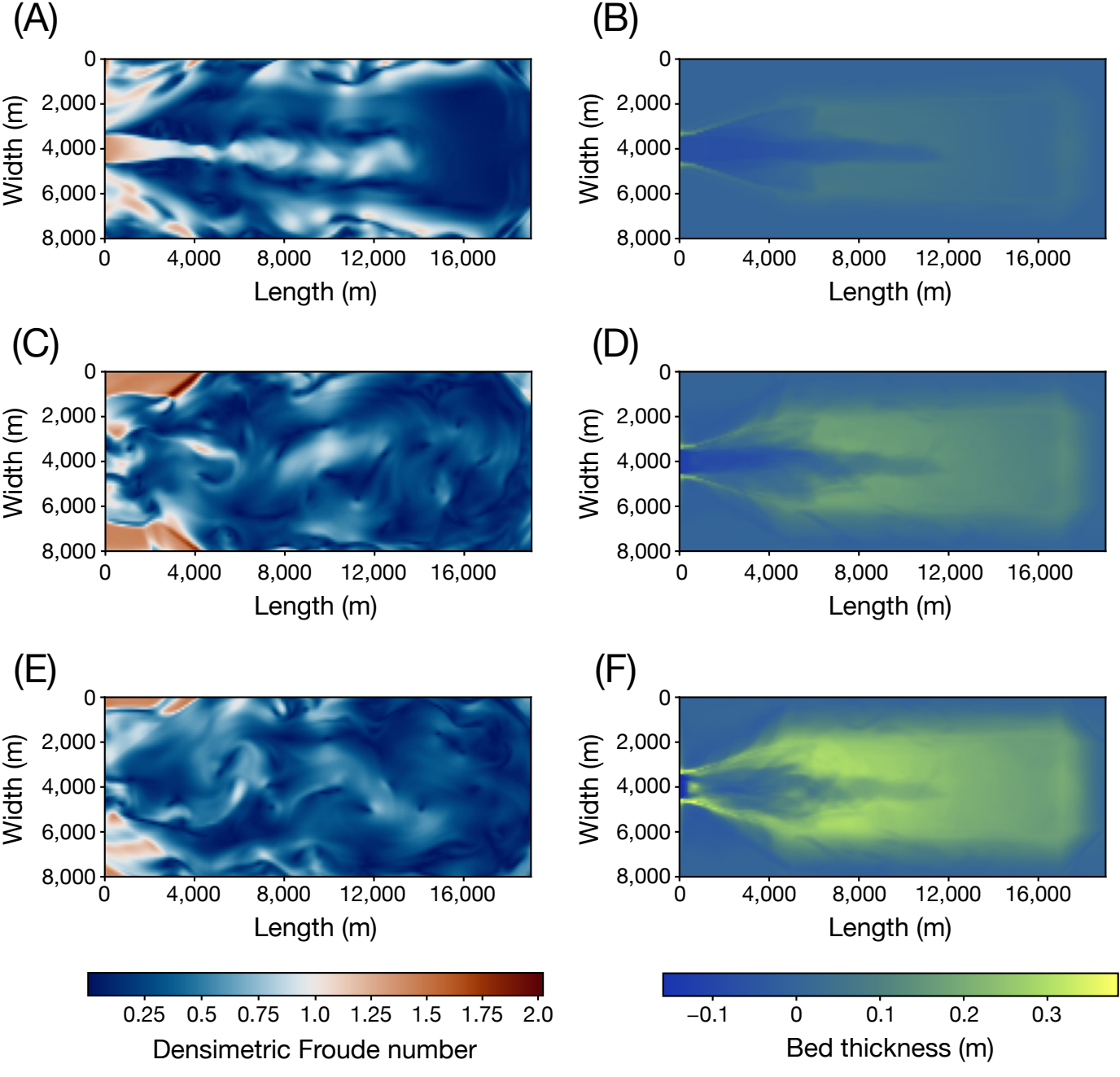
(A)
(B)
(C)
(D)
(E)
(F)
Width (m)
0
2,000
4,000
6,000
8,000
0
4,000
8,000
12,000
16,000
Length (m)
0.25
0.5
0.75
1.0
1.25
1.5
1.75
2.0
Densimetric Froude number
−0.1
0
0.1
0.2
0.3
Bed thickness (m)

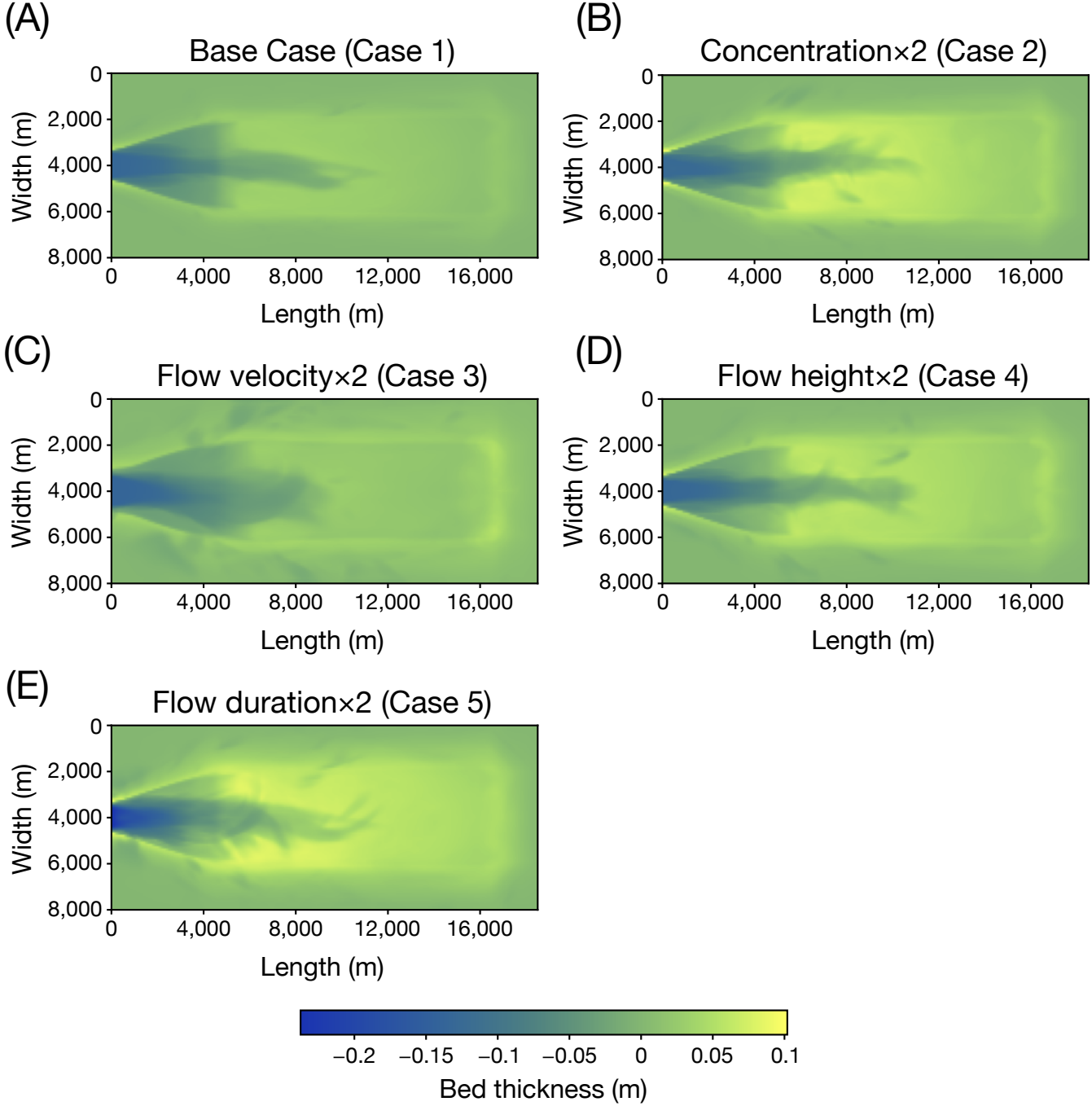
(A)
Base Case (Case 1)
(B)
Concentration×2 (Case 2)
(C)
Flow velocity×2 (Case 3)
(D)
Flow height×2 (Case 4)
(E)
Flow duration×2 (Case 5)
Width (m)
0
2,000
4,000
6,000
8,000
Length (m)
0
4,000
8,000
12,000
16,000
−0.2
−0.15
−0.1
−0.05
0
0.05
0.1
Bed thickness (m)

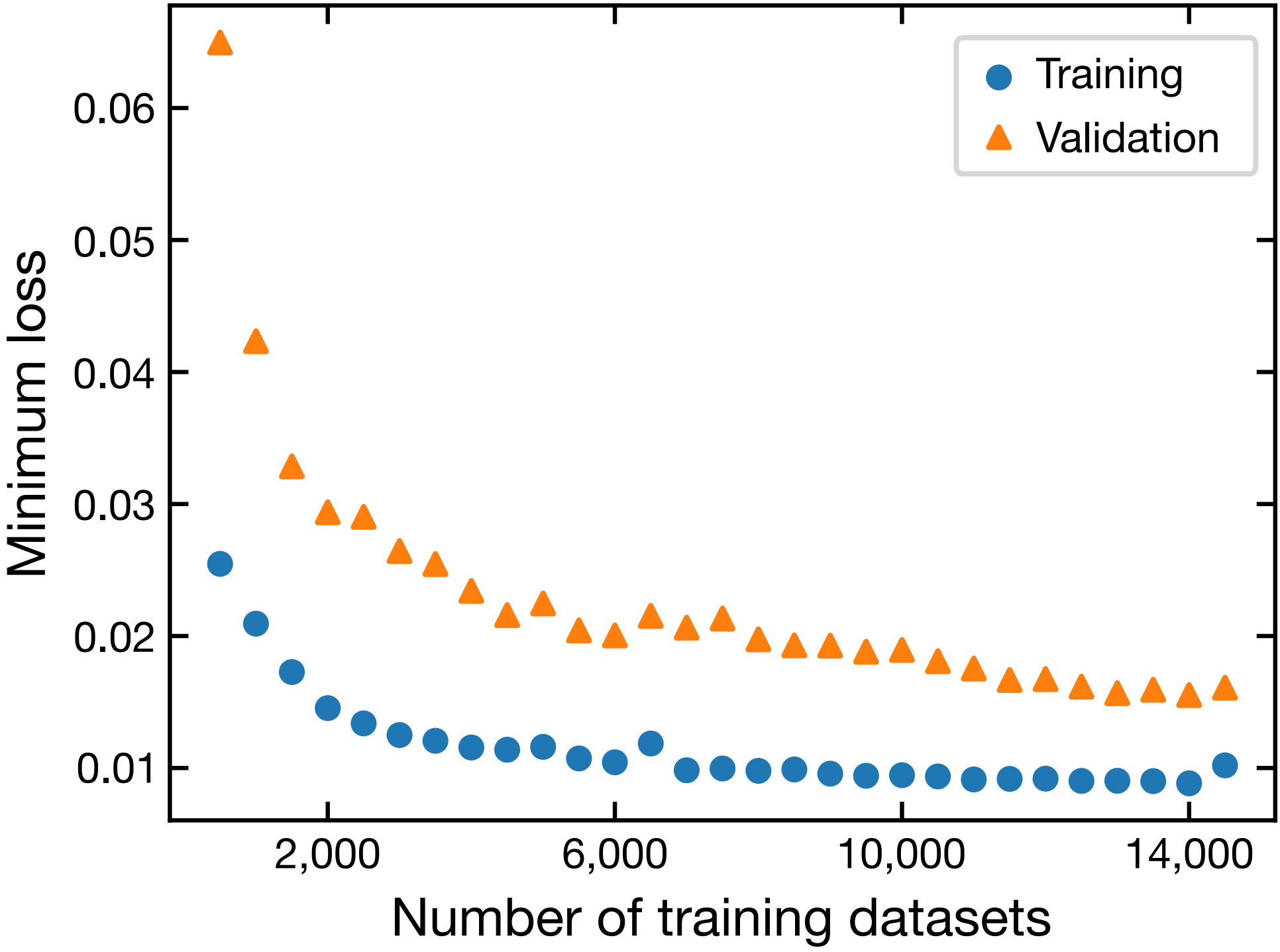
Training
Validation
Minimum loss
0.06
0.05
0.04
0.03
0.02
0.01
2,000
6,000
10,000
14,000
Number of training datasets

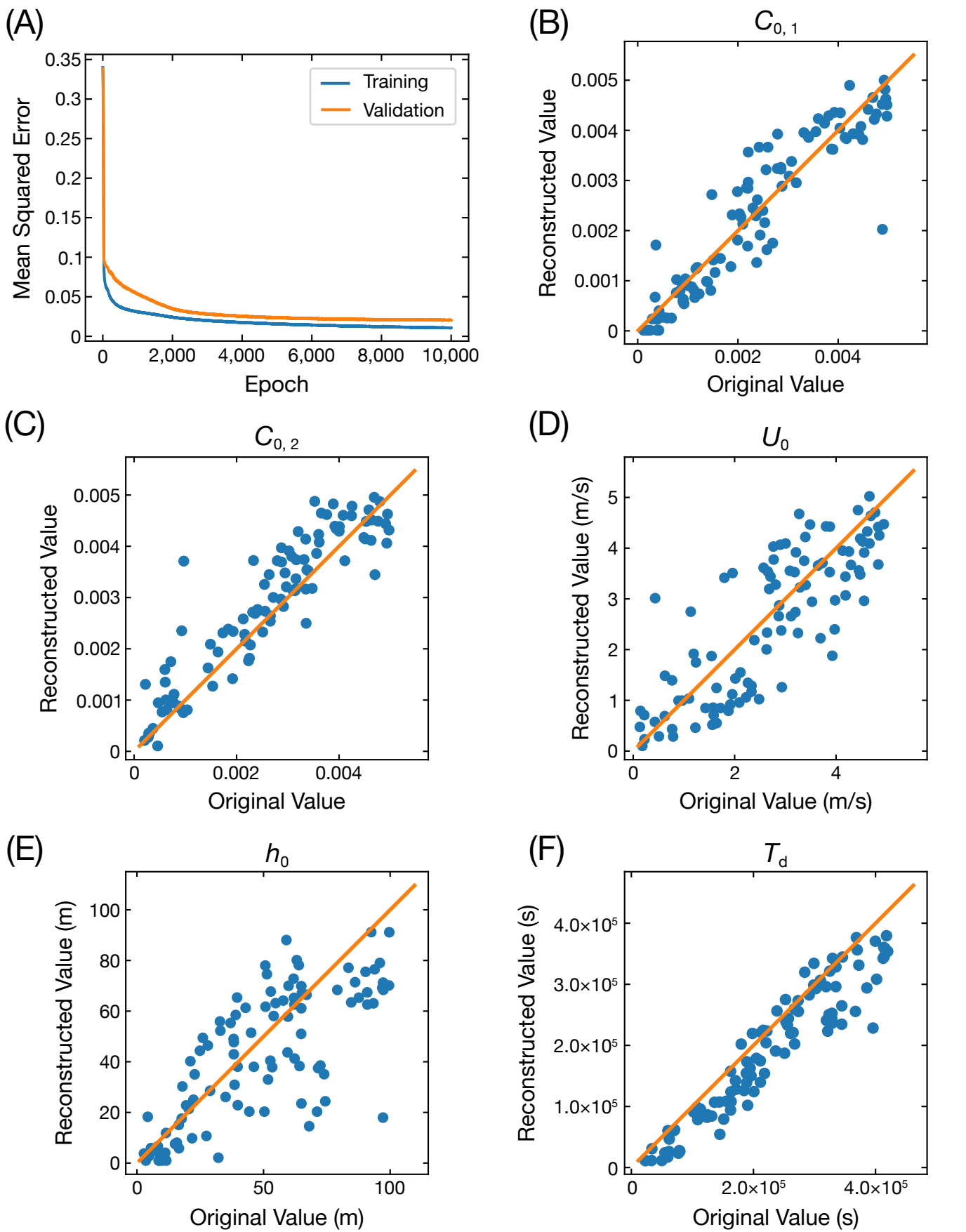
(A)
Mean Squared Error
Epoch
Training
Validation
(B)
$C_{0,1}$
Reconstructed Value
Original Value
(C)
$C_{0,2}$
Reconstructed Value
Original Value
(D)
U_0
Reconstructed Value (m/s)
Original Value (m/s)
(E)
h_0
Reconstructed Value (m)
Original Value (m)
(F)
T_d
Reconstructed Value (s)
Original Value (s)

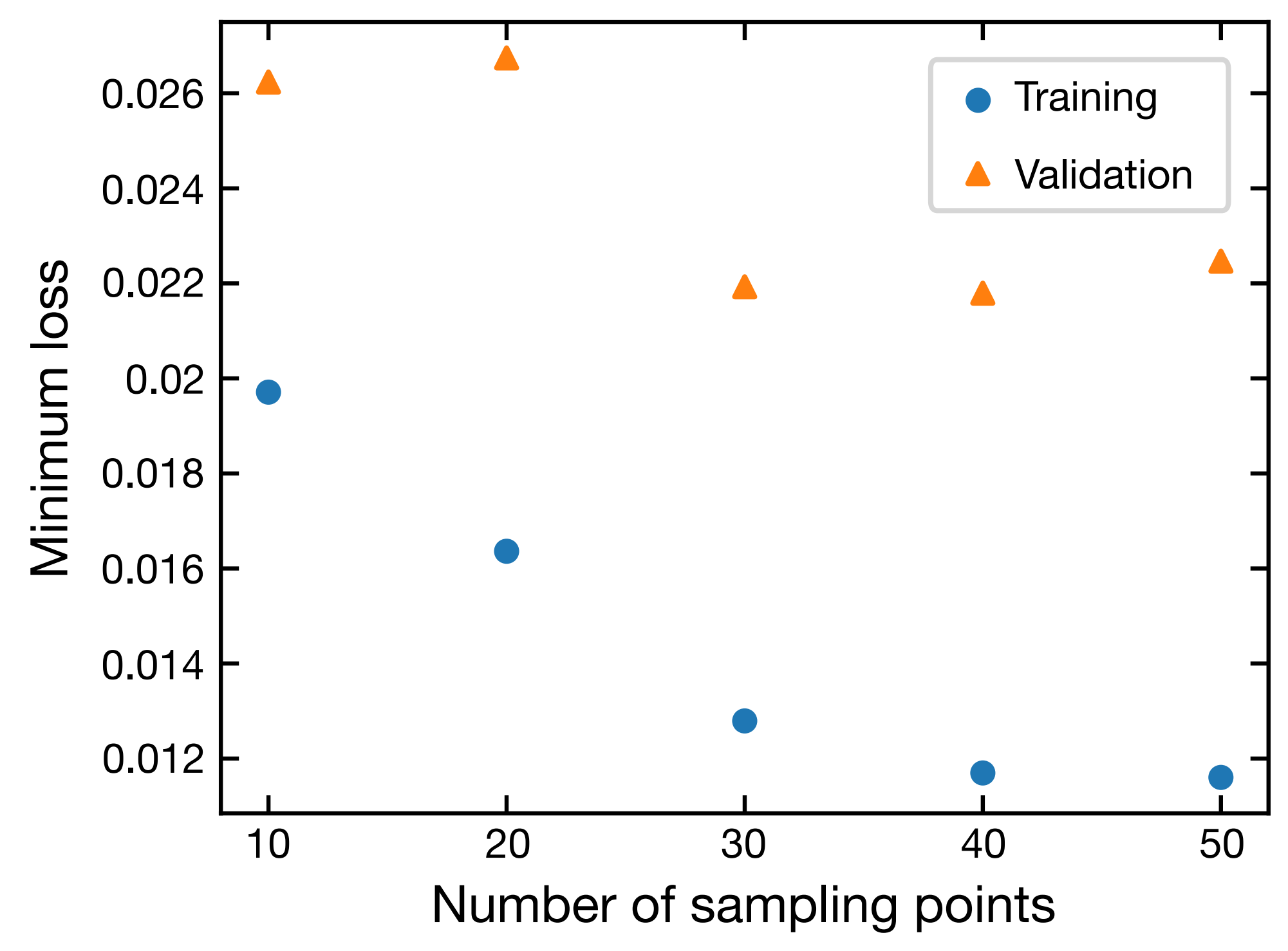
Training
Validation
Minimum loss
0.026
0.024
0.022
0.02
0.018
0.016
0.014
0.012
10
20
30
40
50
Number of sampling points

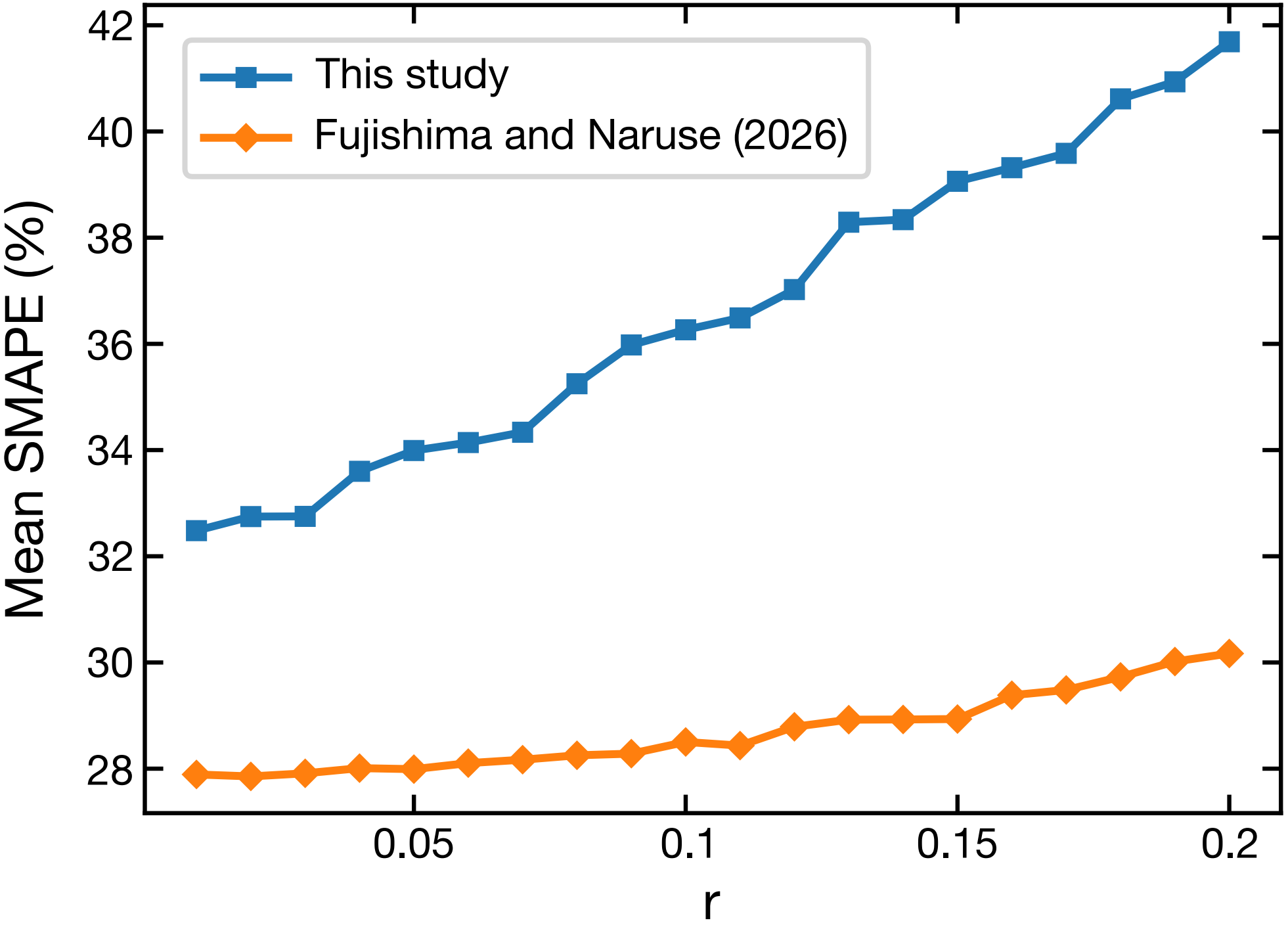
This study
Fujishima and Naruse (2026)
Mean SMAPE (%)
42
40
38
36
34
32
30
28
0.05
0.1
0.15
0.2
r

TABLE 1. Input parameters for the forward model used in the sensitivity test.

	Case 1	Case 2	Case 3	Case 4	Case 5
$C_{0,1}$ (20 μm)	0.001	0.002	0.001	0.001	0.001
$C_{0,2}$ (3 μm)	0.001	0.002	0.001	0.001	0.001
U_0 (m/s)	2.0	2.0	4.0	2.0	2.0
h_0 (m)	4.0	4.0	4.0	8.0	4.0
T_d (s)	200,000	200,000	200,000	200,000	400,000

TABLE 2. Ranges of input parameters for the forward model used to generate the training datasets.

	Min Value	Max Value
$C_{0,i}$	0.00001	0.005
U_0 (m/s)	0.1	5.0
h_0 (m)	1.0	100.0
T_d (s)	1800	432,000

TABLE 3. SMAPE, RMSE, and bias for predicted values obtained by inversion on the test datasets.

	$C_{0,1}$ (20 μm)	$C_{0,2}$ (3 μm)	U_0	h_0	T_d
SMAPE	32.0%	21.9%	36.8%	45.0%	27.4%
RMSE	0.000575	0.000618	0.855 m/s	20.5 m	50,290 s
bias	−0.0000274	0.000259	−0.152 m/s	−6.09 m	−35,674 s

Appendix

Deep Neural Network-Based Inversion of Turbidites in Confined Basins

Seiya Fujihsima[1*] and Hajime Naruse[1]

[1] Department of Geology and Mineralogy, Division of Earth and Planetary Sciences, Graduate School of Science, Kyoto University, Kyoto, Japan

*Corresponding author (E-mail address: fujishima.seiya.z47@kyoto-u.jp)

FORWARD MODEL

Numerical Model of Turbidity Currents Based on Shallow-Water Equations

We employed a horizontally two-dimensional forward model based on the four-equation model (Parker et al. 1986). This model is based on the shallow-water equations, which consider layer-averaged flow parameters. The governing equations for turbidity currents consist of fluid mass conservation, suspended sediment mass conservation, fluid momentum conservation, and turbulent kinetic energy conservation, and are expressed as follows:

$$\frac{\partial h}{\partial t}+\frac{\partial Uh}{\partial x}+\frac{\partial Vh}{\partial y}=e_{\mathrm{w}}\sqrt{U^2+V^2}-d_w \tag{1}$$

$$\frac{\partial C_i h}{\partial t}+\frac{\partial UC_i h}{\partial x}+\frac{\partial VC_i h}{\partial y}=w_{si}(F_i e_{si}-r_0 C_i) \tag{2}$$

$$\frac{\partial Uh}{\partial t}+\frac{\partial U^2 h}{\partial x}+\frac{\partial UVh}{\partial y}=-\frac{1}{2}Rg\frac{\partial C_i h^2}{\partial \mathrm{x}}+RgC_{\mathrm{T}}\frac{\partial \eta_{\mathrm{T}}}{\partial x} -c_{\mathrm{f}}U\sqrt{U^2+V^2}+\nu_{\mathrm{t}}\left(\frac{\partial^2 Uh}{\partial x^2}+\frac{\partial^2 Vh}{\partial y^2}\right) \tag{3}$$

$$\frac{\partial Vh}{\partial t}+\frac{\partial Vh}{\partial x}+\frac{\partial V^2h}{\partial y}=-\frac{1}{2}Rg\frac{\partial C_ih^2}{\partial y}+RgC_{\mathrm{T}}\frac{\partial \eta_{\mathrm{T}}}{\partial y}$$
$$-c_{\mathrm{f}}V\sqrt{U^2+V^2}+\nu_{\mathrm{t}}\left(\frac{\partial^2 Uh}{\partial x^2}+\frac{\partial^2 Vh}{\partial y^2}\right) \quad (4)$$

$$\frac{\partial Kh}{\partial t}+\frac{\partial UKh}{\partial x}+\frac{\partial VKh}{\partial y}=\left\{c_{\mathrm{f}}+\frac{1}{2}(e_{\mathrm{w}}-d_{\mathrm{w}})\right\}(U^2+V^2)^{\frac{3}{2}}-\epsilon_0 h-Rgw_{si}C_{\mathrm{T}}h$$
$$-\frac{1}{2}RgC_{\mathrm{T}}h(e_{\mathrm{w}}-d_{\mathrm{w}})\sqrt{U^2-V^2}-\frac{1}{2}Rghw_{si}(e_{si}-r_0C_{\mathrm{T}}) \quad (5)$$

Here, x and y represent the bed-attached horizontal Cartesian coordinates, respectively, and t represents time. The flow thickness is denoted by h. The parameters C_i and C_{T} denote the layer-averaged suspended sediment concentration in the ith grain-size class and the total suspended sediment concentration, respectively, and U and V are layer-averaged flow velocities of x and y directions, respectively. The layer-averaged turbulent kinetic energy is represented by K. The empirical relationship proposed by Parker et al. (1987) is employed as the coefficient of water entrainment e_{w}, which is expressed as:

$$e_{\mathrm{w}}=\frac{0.075}{\sqrt{1+718R_i^{2.4}}}, \quad (6)$$

where R_i represents the bulk Richardson number, which is defined as:

$$R_i=\frac{RgC_{\mathrm{T}}h}{U^2+V^2}. \quad (7)$$

Here, the submerged specific density of sediment particles $R=(\rho_{\mathrm{s}}/\rho_{\mathrm{f}}-1)$ and the gravitational acceleration are set to 1.65 and 9.81 m/s^2, respectively. The water detrainment rate d_{w} was calculated as a weighted average of the settling velocities of each grain-size class, using the layer-averaged suspended sediment concentration C_i as the weighting factor:

$$d_{\mathrm{w}} = \gamma \sum_i w_{si} C_i \,, \tag{8}$$

where γ is the coefficient of the water detrainment rate, set to 3.05 (Salinas et al. 2019), and w_{si} denotes the settling velocity of sediment particles in the ith grain-size class, calculated using the empirical relationship proposed by Ferguson and Church (2004):

$$w_{si} = \frac{RgD_i^2}{X_1 \nu + (0.75 X_2 RgD_i^3)^{0.5}}. \tag{9}$$

The kinematic viscosity of water, ν, was set to 1.0×10^{-6} m^2/s, corresponding to its value at 20 °C (Lemmon and Harvey 2023). The coefficients X_1 and X_2 were set to 18.0 and 1.0, respectively (Ferguson and Church 2004). The dimensionless sediment entrainment coefficient for the ith grain-size class, e_{si}, is given by the following empirical relationship (Kostic and Parker 2006):

$$e_{si} = p \frac{aZ^5}{1 + \frac{1}{0.3} Z^5}, \tag{10}$$

$$Z = \alpha_1 \frac{u_*}{w_{si}} Re_{\mathrm{p}i}^{\alpha_2}, \tag{11}$$

$$(\alpha_1, \alpha_2) = \begin{cases} (0.586, 1.23) & Re_{\mathrm{p}i} \le 2.36 \\ (1.0, 0.6) & Re_{\mathrm{p}i} > 2.36 \end{cases}, \tag{12}$$

where $a = 1.3 \times 10^{-7}$. The coefficient p represents the strength of the bed sediment and was set to 0.1 in this study. The bed shear velocity u_* is related to the turbulent kinetic energy K as follows:

$$u_* = \sqrt{\alpha K} = \sqrt{c_{\mathrm{f}}}(U^2 + V^2), \tag{13}$$

where the basal friction coefficient c_{f} and α were taken as 0.004 (Kostic and Parker 2006; Fujishima and Naruse 2026) and 0.6 (Salinas et al. 2019), respectively. The parameter r_0, representing the ratio of the near-bed concentration to the layer-averaged

concentration, was set to 2.0 (Kostic and Parker 2006). The particle Reynolds number $Re_{\mathrm{p}i}$ is defined as

$$Re_{\mathrm{p}i} = \frac{\sqrt{RgD_{si}}D_{si}}{\nu}.$$

The parameter ν_{t} is the horizontal eddy viscosity, which is expressed using the following empirical formulation:

$$\nu_{\mathrm{t}} = \frac{1}{6}\kappa u_* h, \tag{14}$$

where κ is the von Kármán constant and was set to 0.4. The mean dissipation rate of the layer-averaged turbulent kinetic energy, ϵ_0, is given by:

$$\epsilon_0 = \beta\frac{K^{1.5}}{h}, \tag{15}$$

where

$$\beta = \frac{\alpha^{1.5}}{\sqrt{c_{\mathrm{f}}}}. \tag{16}$$

Equation (16) is based on the Equation (29) in Fujishima and Naruse (2026).

The sediment mass conservation at the bed and in the active layer take the following forms:

$$\frac{\partial \eta_i}{\partial t} = \frac{w_{si}(r_0 C_i - F_i e_{si})}{1-\lambda_{\mathrm{p}}}, \tag{17}$$

$$\frac{\partial \eta_{\mathrm{T}}}{\partial t} = \sum_i \frac{\partial \eta_i}{\partial t}, \tag{18}$$

$$\frac{\partial F_i}{\partial t} + \frac{F_i}{L_{\mathrm{a}}}\frac{\partial \eta_{\mathrm{T}}}{\partial t} = \frac{w_{si}}{L_{\mathrm{a}}(1-\lambda_{\mathrm{p}})}(r_0 C_i - F_i e_{si}). \tag{19}$$

Here, the total bed thickness and the sediment volume per unit area of ith grain-size class are denoted by η_{T} and η_i, respectively. The parameter F_i represents the volume fraction

of ith grain-size class in the active layer. The porosity of the bed sediment, λ_p, was set to 0.4, and the thickness of the active layer, L_a, was assumed to be constant at 0.01 m (Cai 2022).

Numerical Scheme

The forward model was implemented using the open-source software *turb2d* (Naruse 2020), which employs the CIP-CUP method as its numerical scheme (Yabe and Wang 1991). The advection and pressure terms of the governing equations are solved using the CIP method and an implicit method, respectively, whereas the non-advection terms, and the sediment mass conservation equations of the bed and the active layer are solved using the semi-implicit Euler method. In addition, the model employs the artificial viscosity (Jameson et al. 1981; Ogata and Yabe 1999), and the wet-dry boundary treatment proposed by Yang et al. (2016).

The time step was determined to satisfy the Courant-Friedrichs-Lewy (CFL) condition as follows (Gunawan 2015):

$$\Delta t = \frac{c\Delta \mathrm{x}}{\max\left(|U| + \sqrt{RgC_{\mathrm{T}}h},\ |V| + \sqrt{RgC_{\mathrm{T}}h},\ 1\right)}, \tag{20}$$

where Δt and Δx are the time step and grid spacing, respectively. The parameter c denotes the Courant number, which is typically set to a value less than unity to ensure numerical stability. In this study, c was set to 0.4.

ARCHITECTURE OF DNN-BASED INVERSE MODEL

The inverse models were implemented as fully connected deep neural networks (DNNs). The DNN-based inverse models were designed to take sediment volumes per unit area at the sampling points as input and to output the input parameters of the forward model. The input layer had a number of nodes corresponding to the number of sampling points,

100 followed by 4 hidden layers with 4,000 nodes each, and an output layer with a number of
101 nodes corresponding to the number of input parameters in the forward model. The
102 activation function used in both the hidden and the output layer was rectified linear unit
103 (ReLU) (Nair and Hinton 2010). Training was performed to minimize the mean squared
104 error between the true and predicted input parameters, using Adagrad as the optimization
105 method (Duchi et al. 2011) with a learning rate of 0.01. In addition, to prevent overfitting,
106 dropout was applied to the hidden layers, and 50% of the nodes in the hidden layers were
107 randomly deactivated during training. The training was conducted for 10,000 epochs with
108 a batch size of 64, and the training datasets were split into an 80% training set and a 20%
109 validation set.

110 **REFERENCES**

111 Cai, Z., 2022, Reconstructing the Behavior of Turbidity Currents From
112 Turbidites-Reference to Anno Formation and Japan Trench [Ph.D. Thesis]: Kyoto
113 University, 162 p., doi:https://doi.org/10.14989/doctor.k24174.

114 Duchi, J., Hazan, E., and Singer, Y., 2011, Adaptive Subgradient Methods for
115 Online Learning and Stochastic Optimization: Journal of Machine Learning Research, v.
116 12, p. 2121–2159.

117 Ferguson, R.I., and Church, M., 2004, A Simple Universal Equation for Grain
118 Settling Velocity: Journal of Sedimentary Research, v. 74, p. 933–937,
119 doi:10.1306/051204740933.

120 Fujishima, S., and Naruse, H., 2026, Experimental Verification of a Two-
121 Dimensional Inverse Method for Turbidity Currents Using a Deep Neural Network:
122 Journal of Geophysical Research: Machine Learning and Computation, v. 3, p.
123 e2025JH000952, doi:10.1029/2025JH000952.

Gunawan, H.P., 2015, Numerical simulation of shallow water equations and related models [Ph.D Thesis]: Université Paris-Est; Institut teknologi Bandung, 140 p.

Jameson, A., Schmidt, W., and Turkel, E., 1981, Numerical solution of the Euler equations by finite volume methods using Runge Kutta time stepping schemes: 14th Fluid and Plasma Dynamics Conference, AIAA Meeting Paper, doi:10.2514/6.1981-1259.

Kostic, S., and Parker, G., 2006, The response of turbidity currents to a canyon–fan transition: internal hydraulic jumps and depositional signatures: Journal of Hydraulic Research, v. 44, p. 631–653, doi:10.1080/00221686.2006.9521713.

Lemmon, E.W., and Harvey, A.H., 2023, Thermophysical properties of water and steam, *in* Rumble, J.R. ed., CRC Handbook of Chemistry and Physics: CRC Press.

Nair, V., and Hinton, G.E., 2010, Rectified Linear Units Improve Restricted Boltzmann Machines: The 27th international conference on machine learning, Proceedings of the 27th international conference on machine learning, p. 807–814.

Naruse, H., 2020, Numerical simulation of turbidity current by open source software “turb2d”: Journal of the Sedimentological Society of Japan, v. 78, p. 54, doi:10.4096/jssj.78.54.

Ogata, Y., and Yabe, T., 1999, Shock capturing with improved numerical viscosity in primitive Euler representation: Computer Physics Communications, v. 119, p. 179–193, doi:10.1016/s0010-4655(99)00188-5.

Parker, G., Fukushima, Y., and Pantin, H.M., 1986, Self-accelerating turbidity currents: Journal of Fluid Mechanics, v. 171, p. 145–181, doi:10.1017/S0022112086001404.

Parker, G., Garcia, M., Fukushima, Y., and Yu, W., 1987, Experiments on turbidity currents over an erodible bed: Journal of Hydraulic Research, v. 25, p. 123–147,

doi:10.1080/00221688709499292.

Salinas, J.S., Cantero, M.I., Shringarpure, M., and Balachandar, S., 2019, Properties of the Body of a Turbidity Current at Near-Normal Conditions: 2. Effect of Settling: Journal of Geophysical Research: Oceans, v. 124, p. 8017–8035, doi:10.1029/2019JC015335.

Yabe, T., and Wang, P.-Y., 1991, Unified Numerical Procedure for Compressible and Incompressible Fluid: Journal of The Physical Society of Japan, v. 60, p. 2105–2108, doi:https://doi.org/10.1143/JPSJ.60.2105.

Yang H., Lu M., and Kumakura T., 2016, A study on the water front in shallow water equations: Journal of Japan Society of Civil Engineers, Ser. B1 (Hydraulic Engineering), v. 72, p. I_325–I_330, doi:10.2208/jscejhe.72.i_325.